PHYSICAL REVIEW B **93**, 125434 (2016)

Photon drag effect in $(Bi_{1-x}Sb_x)_2Te_3$ three-dimensional topological insulators

H. Plank,[1] L. E. Golub,[2] S. Bauer,[1] V. V. Bel'kov,[2] T. Herrmann,[1] P. Olbrich,[1] M. Eschbach,[3] L. Plucinski,[3] C. M. Schneider,[3] J. Kampmeier,[3] M. Lanius,[3] G. Mussler,[3] D. Grützmacher,[3] and S. D. Ganichev[1]

[1]*Terahertz Center, University of Regensburg, 93040 Regensburg, Germany*

[2]*Ioffe Institute, 194021 St. Petersburg, Russia*

[3]*Peter Grünberg Institute (PGI) and Jülich Aachen Research Alliance (JARA-FIT), 52425 Jülich, Germany*

(Received 22 December 2015; published 29 March 2016)

We report on the observation of a terahertz radiation-induced photon drag effect in epitaxially grown *n*- and *p*-type $(Bi_{1-x}Sb_x)_2Te_3$ three-dimensional topological insulators with different antimony concentrations x varying from 0 to 1. We demonstrate that the excitation with polarized terahertz radiation results in a dc electric photocurrent. While at normal incidence a current arises due to the photogalvanic effect in the surface states, at oblique incidence it is outweighed by the trigonal photon drag effect. The developed microscopic model and theory show that the photon drag photocurrent can be generated in surface states. It arises due to the dynamical momentum alignment by time- and space-dependent radiation electric field and implies the radiation-induced asymmetric scattering in the electron momentum space. We show that the photon drag current may also be generated in the bulk. Both surface states and bulk photon drag currents behave identically upon variation of such macroscopic parameters as radiation polarization and photocurrent direction with respect to the radiation propagation. This fact complicates the assignment of the trigonal photon drag effect to a specific electronic system.

DOI: 10.1103/PhysRevB.93.125434

I. INTRODUCTION

Much attention in condensed-matter physics is currently directed towards understanding electronic properties of Dirac fermions in three-dimensional (3D) topological insulators (TIs), which challenge fundamental concepts and hold great potential for electronic, optic, and optoelectronic applications (see, e.g., Refs. [1–9]).

Recently, nonlinear high-frequency electron transport phenomena [10–13] in TI systems have attracted growing interest. There have been many theoretical and experimental works in the past few years on helicity-controlled photocurrents [14–18], the linear photogalvanic effect [19–21], local photocurrents [22,23], edge photocurrents in two-dimensional (2D) TIs [24,25], coherent control of injection currents [26,27], photon drag currents [19,28,29], second-harmonic generation [30], photoinduced quantum Hall insulators [31,32], cyclotron-resonance-assisted photocurrents [33,34], quantum oscillations of photocurrents [35], photogalvanic currents via proximity interactions with magnetic materials [36–38], and the photoelectromagnetic effect [39]. These phenomena, scaling in the second or third order of the radiation electric fields, open up new opportunities to study Dirac fermions, which has been already demonstrated for graphene (for a review see Ref. [13]) and several TI materials (see, e.g., Refs. [15,19,23,34]). An important advantage of the nonlinear high-frequency transport effects is that some of them, being forbidden by symmetry in the bulk of most 3D TIs, can be applied to selectively probe the surface states even in TI materials with a finite bulk conductivity. Utilizing photocurrents, this advantage has been used to study Sb_2Te_3 and Bi_2Te_3 3D TIs [19], in which conventional dc transport experiments, particularly at room temperature, are handicapped by a large residual bulk charge-carrier density [40–45].

It has been shown in Ref. [19] that the photocurrent excited by normal incident terahertz (THz) radiation is generated due to the photogalvanic effect. The latter originated from the asymmetric scattering of Dirac fermions driven back and forth by the ac electric field and is allowed only in the noncentrosymmetric surface states. The experiments further hinted at a possible contribution of the photon drag effect, a competing photocurrent resulting from the light momentum transfer to charged carriers. However, no experiments which provide clear evidence of the photon drag effect in TI materials have been reported so far.

Here we report on the observation of the photon drag effect in $(Bi_{1-x}Sb_x)_2Te_3$ 3D TIs excited by THz radiation. We demonstrate that while at normal incidence the photocurrent is dominated by the photogalvanic effect, at oblique incidence it is outweighed by the photon drag effect. The latter is shown to be caused by the *in-plane* component of the photon wave vector $\boldsymbol{q}_\parallel$. Strikingly, the observed photon drag current does not change its sign upon inverting $\boldsymbol{q}_\parallel$. This seemingly surprising result is caused by the fact that in materials with trigonal symmetry the photon drag current is proportional not only to the photon wave vector but also to the product of *in-* and *out-of-plane* components of the radiation electric field. Since both $\boldsymbol{q}_\parallel$ and the product of the electric fields change their sign, the total sign remains unchanged. Importantly, the trigonal photon drag effect can be generated in the surface states as well as in the bulk, being described by the same phenomenological equation. Our experimental findings are well described by the developed theory and microscopic model based on the Boltzmann kinetic equation for the carrier distribution function. Both photon drag and photogalvanic effects are investigated in epitaxially grown $(Bi_{1-x}Sb_x)_2Te_3$ bulk materials of various compositions determined by the antimony content x. The variation of x enabled us to study photocurrents in different systems, including binary and ternary TIs with smooth changes from *n*- to *p*-type bulk conductivity (see Refs. [46,47]), as well as in heterostructure samples, consisting of an *n*-type Bi_2Te_3 and a *p*-type Sb_2Te_3 layer (see Ref. [48]). In the latter the chemical

TABLE I. Sample parameters and the amplitudes of photocurrents A_x excited by normal incident radiation with $f = 3.3$ THz. Angles of incidence $\theta = 0$ and 180° correspond to the front and back excitation, respectively.

Sample ID	Type	Structure	Sb content x	Type Bulk carriers	A_x (nA cm^2/W) $\theta = 0$	A_x (nA cm^2/W) $\theta = 180°$
BST127	binary	20 nm Bi_2Te_3	0	n	0.32	0.8
BST307	binary	13 nm Bi_2Te_3	0	n	3.1	7
BST323	ternary	24 nm $(Bi_{1-x}Sb_x)_2Te_3$	25	n	1.8	
BST306	ternary	23 nm $(Bi_{1-x}Sb_x)_2Te_3$	40	n	0.06	0.04
BST641	ternary	175 nm $(Bi_{1-x}Sb_x)_2Te_3$	43	n	0.4	0.6
BST305	binary	27 nm Sb_2Te_3	100	p	0.025	0.02
BST508	heterostructure	10 nm n-Bi_2Te_3 +7.5 nm p-Sb_2Te_3	–	–	0.3	

potential can be tuned by varying the thickness of the upper Sb_2Te_3 layer.

II. SAMPLE DESCRIPTION

The samples were grown by molecular beam epitaxy (MBE) on Si(111) substrates in the so-called van der Waals (vdW) growth mode [49]; that is, there are only weak bonds between the substrate and the TI epilayers, so that the large lattice mismatch does not hinder the growth of single-crystal TI films with a high structural quality [50–52]. Before insertion into the MBE chamber, the Si(111) surface was chemically cleaned to remove the native SiO_2 and to passivate the surface with hydrogen. Prior to the TI layer deposition, the substrate was heated up to 600° C for 20 min to desorb the hydrogen atoms. The Bi, Sb, and Te atoms were deposited on the substrate using effusions cells, working at temperatures of 530 °C (Bi), 450 °C (Sb), and 380 °C (Te), whereas the substrate temperature was 300 °C. The Bi_2Te_3 (Sb_2Te_3) layer was deposited with a slow growth rate of 27 nm/h (9 nm/h). The sample BST641 was grown at temperature $T_{Bi} = 470$ °C, $T_{Sb} = 417$ °C, $T_{Te} = 330$ °C, $T_{substrate} = 300$ °C and with a growth rate of 10 nm/h for 1050 min, which corresponds to a thickness of 175 nm. The structure composition and thickness of all investigated samples are given in the Table I. To characterize the samples, electrical measurements on Hall-bar

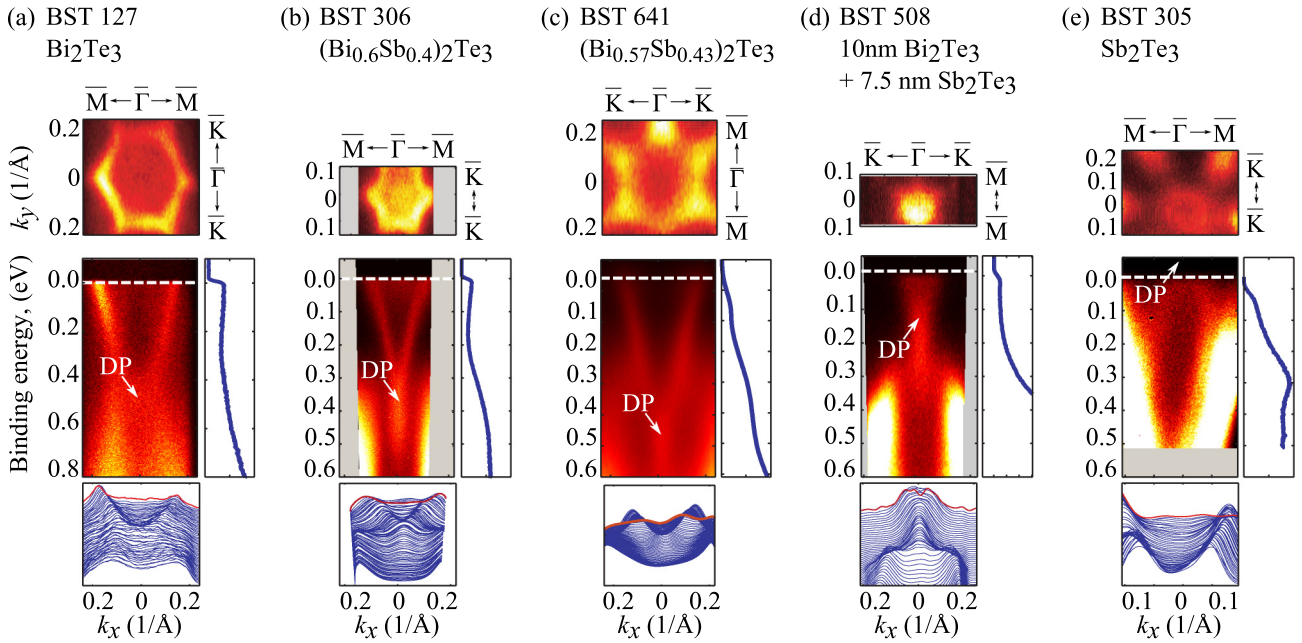

FIG. 1. ARPES investigation of the surface electronic structure of different TI samples, measured at low temperature ($T \approx 25$ K) using photon energy of 8.4 eV. The spectra unambiguously prove the existence of topological surface states in each material. (a) Results for pure n-type Bi_2Te_3. The corresponding results for samples (b) BST306 and (c) BST641, i.e., the n-type $(Bi_{0.6}Sb_{0.4})_2Te_3$ and $(Bi_{0.57}Sb_{0.43})_2Te_3$ ternary TIs, (d) for sample BST508, i.e., the n-type 10-nm Bi_2Te_3/7.5-nm Sb_2Te_3 TI heterostructure, and (e) for sample BST305, i.e., the p-type Sb_2Te_3. The top panels depict the constant-energy contour at $\varepsilon_B = 0$ with indicated crystallographic directions showing the hexagonal warping of the energy spectrum of the topological surface states. The middle panel illustrates the binding-energy-dispersion spectra $\varepsilon(k)$ map at $k_y = 0$ along the $\bar{\Gamma}M$ direction, where the upper part of the topological surface states is revealed while the Dirac point is buried in the bulk valence-band maximum. Additionally, the energy distribution curves, integrated over the entire image, are shown beside the middle panels. The bottom panels depict the respective momentum distribution curves. The ones for $\varepsilon_B = 0$ are highlighted in red.

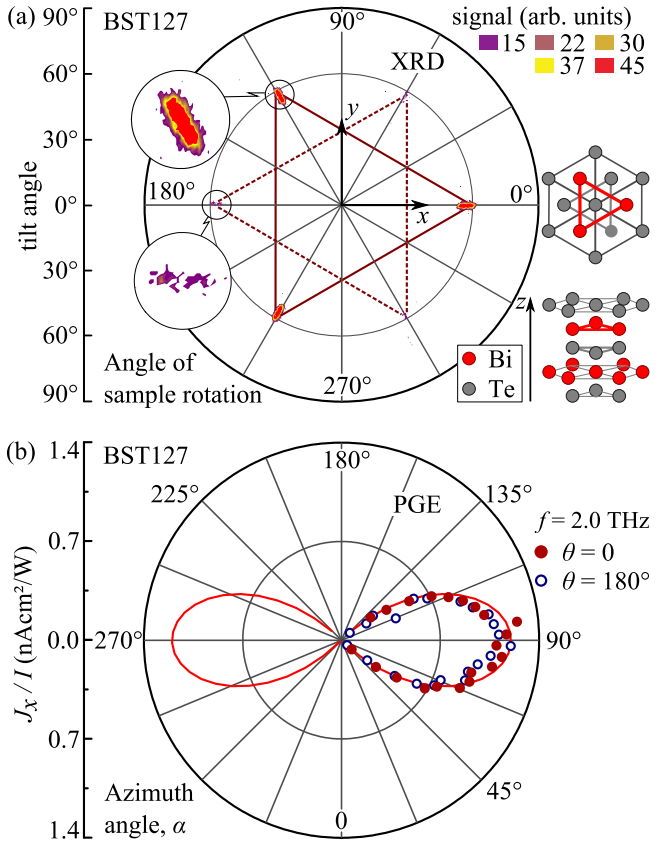

FIG. 2. (a) X-ray-diffraction pole figure scan around the (1,0,5) reflection of the Bi_2Te_3 sample BST127 showing that one domain orientation (highlighted by the solid red line) dominates. It also reveals that the crystallographic axes lie parallel to the sample edges. Insets sketch domain orientations illustrated by the solid red line connecting the top Bi atoms in the top right panel and the side view of one quintuple layer (see the bottom right panel). (b) Photocurrent $J_x(\alpha)/I$ in Bi_2Te_3 sample BST127 measured for front and back illumination at $T = 296$ K. Solid lines show fits after Eq. (1). Note that the same dependencies are obtained after phenomenological [see Eq. (4)] and microscopic theory [see Eq. (19)] for the photogalvanic effect.

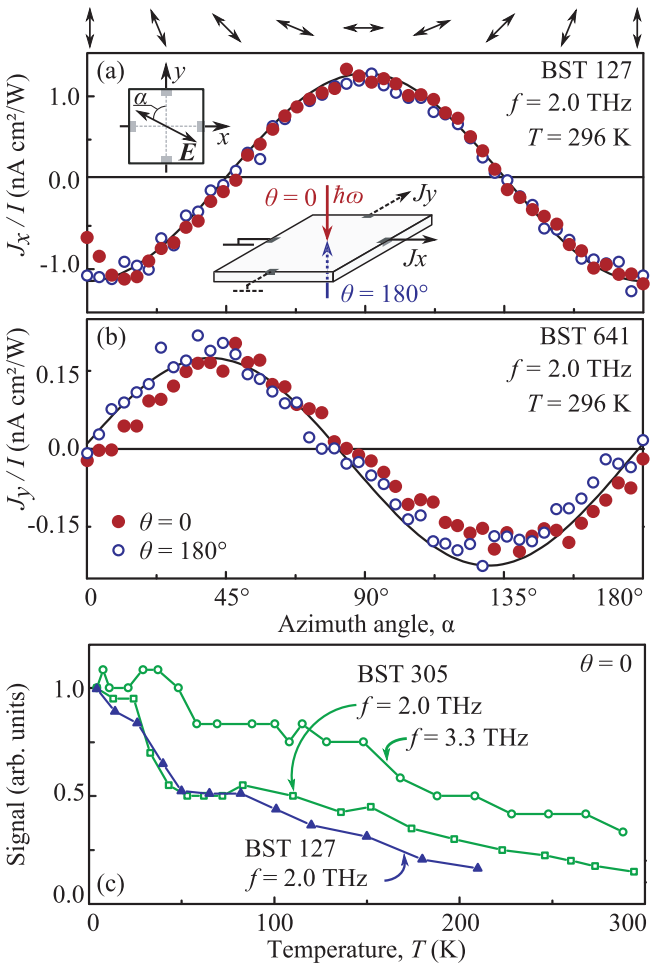

FIG. 3. (a) Photocurrent J_x/I measured in Bi_2Te_3 sample BST127. (b) Photocurrent J_y/I measured in $(Bi_{0.57}Sb_{0.43})_2Te_3$ sample BST641. Plots show the dependence of the photocurrent excited by normal incident radiation with $f = 2.0$ THz on the azimuth angle α. Angles of incidence $\theta = 0$ and 180° correspond to the front and back excitations, respectively. Solid lines show fits after Eq. (1). Note that the same dependencies are obtained after phenomenological [see Eq. (4)] and microscopic theory [see Eqs. (19) and (26) for the photogalvanic and the photon drag effect, respectively]. Insets sketch the setup and the orientation of the electric field. Note that the photocurrent is probed in the directions coinciding with the principal axes of the trigonal system. (c) Temperature dependence of the photocurrent measured in the Bi_2Te_3 sample BST127 and Sb_2Te_3 sample BST305. All data are normalized to the value for $T = 4.2$ K.

structures using a standard four-point probe and lock-in technique were carried out at $T = 1.5$ K. The bulk charge-carrier densities have been determined as follows: For binary n-type Bi_2Te_3 and p-type Sb_2Te_3 the bulk carrier density is $n \approx p \approx 5\times10^{19}$ cm^{-3}. For ternary $(Bi_{1-x}Sb_x)_2Te_3$ alloys with x of about 0.4–0.5 we obtain $n \approx p \approx 5\times10^{18}$ cm^{-3}. The sample $(Bi_{0.57}Sb_{0.43})_2Te_3$ (BST641), the most insulating in the bulk, is n type and has a carrier density of $n = 3\times10^{17}$ cm^{-3}.

The existence of topologically protected surface states has been verified by means of angle -resolved photoemission spectroscopy (ARPES) [53,54] (see Fig. 1). Selected samples have been exposed to air and were transferred into a laboratory-based high-resolution ARPES chamber. In order to remove the oxidized layer and surface contaminants, the samples needed to be cleaned by repeated steps of gentle sputtering using 750 eV Ar ions and annealing to 250 °C to 280 °C. After this cleaning procedure ARPES maps were obtained at low temperatures ($T \approx 25$ K) employing a monochromatized microwave-driven Xe source with a photon energy of 8.4 eV. Topological surface states have been identified in all of the samples (see also Refs. [47,48]). Further, the energetic position of the Dirac point $\varepsilon_B(DP)$ was extracted from the ARPES data. For all samples $\varepsilon_B(DP)$ are on the order of hundreds of meV, comparable with values reported previously for similar materials [46].

Additionally, x-ray diffraction (XRD) measurements were performed in order to verify the single crystallinity of the thin films and the orientation with respect to the Si(111) substrate and to determine the domain orientation (see Fig. 2). The XRD data demonstrate the formation of two trigonal domains, which are mirror symmetric to each other, and

TABLE II. Frequencies and corresponding wavelengths used in the experiments.

	f (THz)					
	3.9	3.3	2.0	1.1	0.8	0.6
λ (μm)	77	90	148	280	385	496

show, however, that the majority of the domains have the same orientation [19,55]. The domains can also be seen in the atomic force microscopy images showing trigonal islands (not shown). Height profiles prove that the quintuple layers (QL) have steps of about 1 nm [19,51]. Using the XRD results, we prepared square-shaped samples with edges cut along crystallographic axes x and y (see Fig. 2). To enable electrical measurements two pairs of Ohmic contacts were prepared in the middle of the 5×5 mm square sample's edges.

III. EXPERIMENTAL TECHNIQUE

Experiments on photocurrents in $(Bi_{1-x}Sb_x)_2Te_3$ 3D TIs were performed while applying radiation from a high-power pulsed molecular THz laser [56,57]. Using NH_3, D_2O, and CH_3F as active gases for the optically pumped laser, 40-ns pulses with a peak power of $P \approx 10$ kW were obtained at different frequencies f (see Table II and Refs. [58–60]). The radiation induces indirect (Drude-like) optical transitions because the photon energies are much smaller than the carrier Fermi energy. The beam had an almost Gaussian form, which was measured by a pyroelectric camera [61,62]. A typical spot diameter depends on the radiation frequency and varies between 1 and 3 mm. The electric field amplitude E_0 of the incoming radiation was varied from about 1 to 30 kV/cm (radiation intensities I from about 1 to 1000 kW/cm^2).

The samples were illuminated at normal and oblique incidence. In experiments at normal incidence front and back illumination was used with an angle of incidence $\theta = 0°$ and 180°, respectively (see Figs. 3 and 4). In the measurements applying oblique incident radiation the angle θ was varied between −35° and 35° (see insets in Figs. 5 and 6). Note that larger angles of incidence were not used in order to avoid the illumination of contacts and edges. The photocurrents were analyzed in two directions, x and y, perpendicular to each other and parallel to the sample edges (see inset in Fig. 3). Most experiments at oblique incidence were carried out for the (yz) plane of incidence. In some additional measurements the orientation of the plane of incidence was rotated by the angle ψ with respect to the (yz) plane (see inset in Figs. 7 and 8).

The dc photocurrent J was excited in the temperature range from $T = 4.2$ to 296 K. It was measured as a voltage drop, $U \propto J$, across a 50 Ω load resistor and recorded in unbiased samples with a storage oscilloscope. To control the incidence power of the laser the signal was simultaneously measured at a reference THz detector [63]. To examine the photocurrent

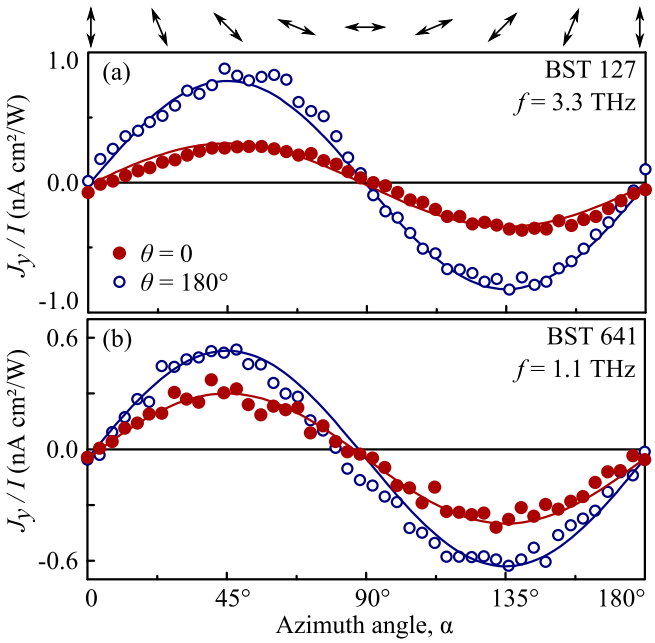

FIG. 4. (a) J_y/I measured in Bi_2Te_3 sample BST127 for $f = 3.3$ THz. (b) J_y/I measured in $(Bi_{0.57}Sb_{0.43})_2Te_3$ sample BST641 for $f = 1.1$ THz. The data show the dependence of the photocurrent on the azimuth angle α excited by normal incident radiation. Angles of incidence $\theta = 0$ and 180° correspond to the front and back excitations, respectively. Solid lines show fits after Eq. (1). Note that the same dependencies are obtained after phenomenological [see Eq. (4)] and microscopic theory [see Eqs. (19) and (25) for the photogalvanic and the q_z-photon drag effects, respectively].

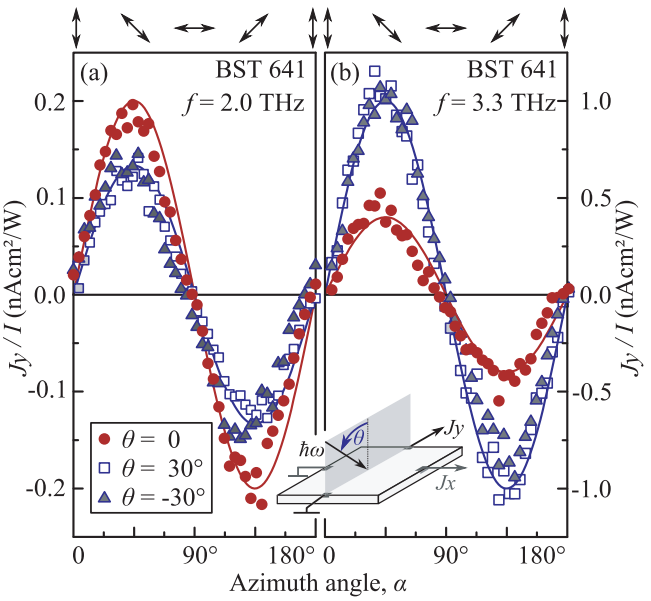

FIG. 5. Azimuth angle dependencies of the photocurrent J_y/I excited in $(Bi_{0.57}Sb_{0.43})_2Te_3$ sample BST641 by normal and oblique incident radiation. The data demonstrate that the polarization dependence does not change upon variation of the angle of incidence either for (a) the case in which the current decreases at oblique incidence ($f = 2.0$ THz) or (b) the case in which it increases with increasing $|\theta|$ ($f = 3.3$ THz). Solid lines show fits after Eq. (1). Note that the same dependencies are obtained after phenomenological [see Eq. (4)] and microscopic theory [see Eqs. (17), (19), and (25) for the photogalvanic and both photon drag effects].

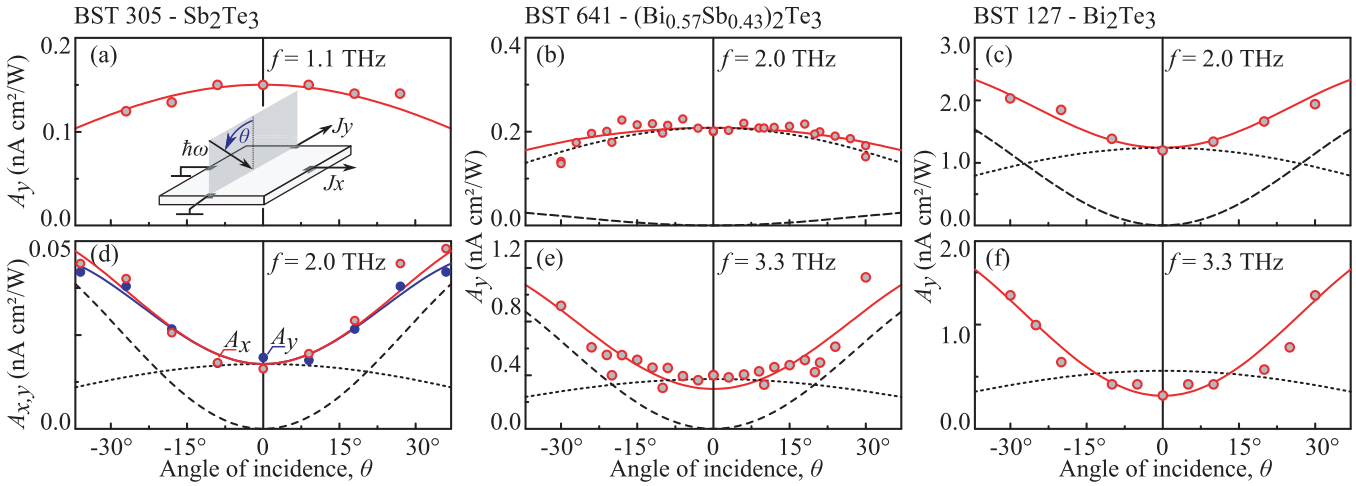

FIG. 6. Dependencies of the photocurrent amplitudes $A_{x,y}$ on the angle of incidence θ obtained for different frequencies and three samples: Sb_2Te_3 (BST305), $(Bi_{0.57}Sb_{0.43})_2Te_3$ (BST641), and Bi_2Te_3 (BST127). Solid lines show fits after Eq. (4) and calculations after Eqs. (19), (25), and (17). Dotted and dashed lines show contributions of the photogalvanic effect and photon drag effect caused by the q_x component of the photon wave vector. The curves are calculated after Eqs. (19) and (17), respectively. Note that solid curves in (e) and (f) are obtained by also taking into account the contribution of the photon drag effects caused by the q_z component of the photon wave vector. The latter effect (not shown) mainly contributes to the signal at normal incidence and is the cause of the difference between the value of the calculated total photocurrent (solid line) and the photogalvanic effect contribution (dotted line). It has a negative sign and decreases with increasing θ. The relative contributions of the photogalvanic and photon drag effects are obtained from the measurements applying front and back illuminations; see Figs. 3 and 4 as well as Table I. The inset in (a) sketches the setup.

behavior upon the variation of the polarization state half- and quarter-wavelength plates were employed. The initial laser radiation was linearly polarized along the y axis. By using $\lambda/2$ plates, the azimuth angle α was varied between the linear polarization of the sample and the y axis (see inset and top panel in Fig. 3).

By applying $\lambda/4$ plates, we obtained elliptically (and circularly) polarized radiation. In this case, the polarization state is determined by the angle φ between the plate optical axis and the incoming laser polarization. Here the electric field vector is lying parallel to the x axis. The polarization states for several φ are shown in the top panel of Fig. 9. In this geometry, the radiation helicity is varied as $P_{\rm circ} = \sin 2\varphi$ [64,65].

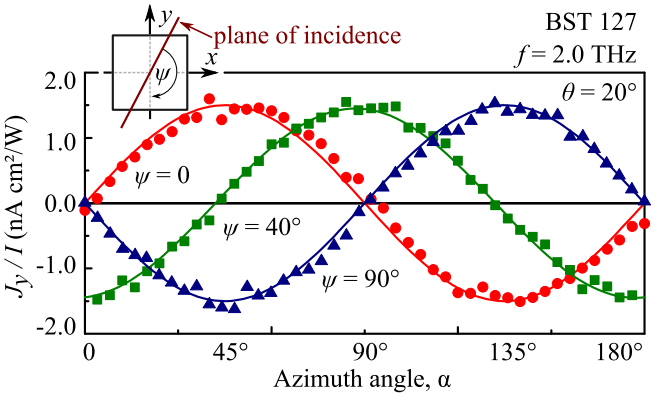

FIG. 7. Azimuth angle dependencies of the photocurrent J_y/I excited in Bi_2Te_3 sample BST127. The data are obtained at oblique incidence radiation ($f = 2.0$ THz) for $\theta = 20°$ and different orientations of the plane of incidence with respect to the y direction given by the angle ψ; see the inset. The data are shown for the angles $\psi = 0°$, 40°, and 90°. The solid lines are calculated after Eq. (5).

IV. EXPERIMENTAL RESULTS

Irradiating the $(Bi_{1-x}Sb_x)_2Te_3$ 3D TIs with linearly polarized THz radiation, we observed a dc current in both the x and y directions. The photocurrent was detected in the whole frequency range used from 0.6 up to 3.9 THz. The signal followed the temporal structure of the laser pulse. Its variation upon rotation of the polarization plane is well fitted by

$$J_x = [-A(f)\cos 2\alpha + C(f)]E_0^2\,,$$
$$J_y = [A(f)\sin 2\alpha + C'(f)]E_0^2, \qquad (1)$$

in which $E_0^2 \propto I$ is the squared radiation electric field and A, C, and C' are fitting parameters [see Figs. 3(a) and 3(b)]. The above polarization dependencies were observed in all samples and for all frequencies. Cooling the sample from room temperature to 4.2 K did increase the photocurrent amplitude [see Fig. 3(c)], whereas the overall behavior remained unchanged.

As we have shown in Ref. [19], two phenomena can be the cause of the THz radiation-induced photocurrents, described by Eqs. (1), namely, the photogalvanic and the photon drag effects [66]. Experiments applying front and back illumination with normally incident radiation allow us to distinguish them from each other. While the photogalvanic current is determined by the in-plane orientation of the radiation electric field [19] and, consequently, remains unchanged for both geometries, the photon drag current is additionally proportional to a component of the photon momentum $\boldsymbol{q}$. Therefore, changing $\boldsymbol{q} \to -\boldsymbol{q}$ (front to back illumination) does not affect the photogalvanic effect but inverts the sign of the factor $A(f)$ for

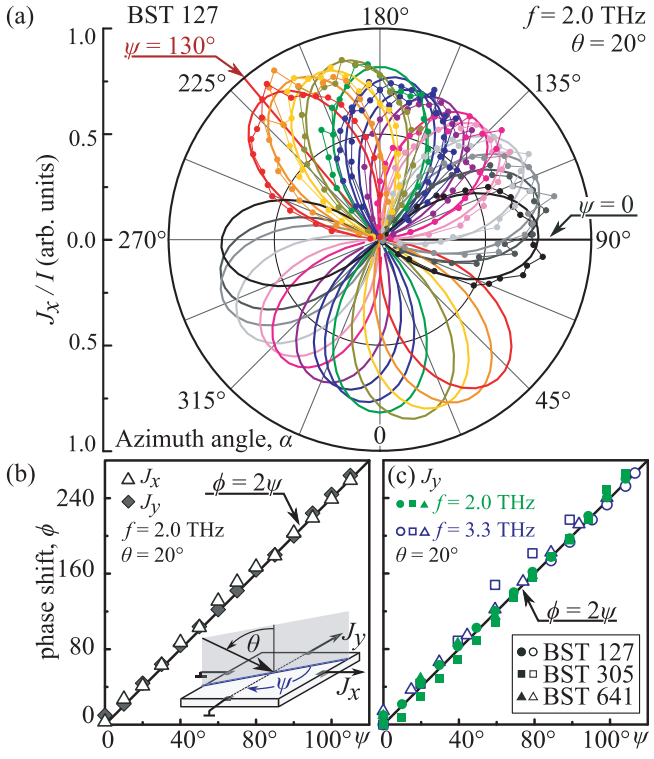

FIG. 8. (a) Azimuth angle dependencies of the photocurrent J_x/I excited in Bi_2Te_3 sample BST127. The data are obtained at oblique incidence radiation ($f = 2.0$ THz) for $\theta = 20°$ and different orientations of the plane of incidence with respect to the y direction given by the angle ψ. The data are shown for the angle ψ changing from 0° to 130° with steps of $\Delta\psi = 10°$. Solid lines show fits after Eqs. (5). The measured phase shift as a function of ψ for (b) the data shown in (a) and (c) samples BST641, BST127, and BST305 and two radiation frequencies. Here solid and open symbols correspond to the frequencies $f = 2.0$ and 3.3 THz, respectively. The solid line shows a fit with $\phi = 2\psi$.

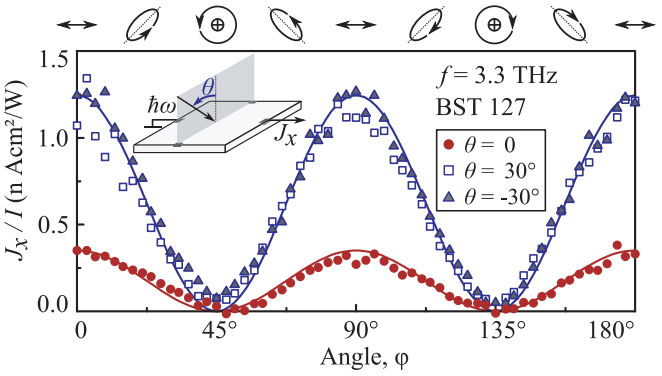

FIG. 9. Helicity dependence of the photocurrent, J_x/I, measured in Bi_2Te_3 sample BST127 at normal as well as oblique incidence in the direction normal to the plane of incidence. The ellipses on top illustrate the polarization states for various angles φ. Solid lines show fits after Eqs. (4), where the polarization-dependent terms take, for this geometry, the form $J_x = A_x(f)(\cos 4\varphi + 1)/2$.

the photon drag effect. Note that for front and back illumination at normal incidence the wave vector $\boldsymbol{q}$ is directed parallel or antiparallel to the z direction. As an important result we found that the sign of the amplitude $A(f)$ remains unchanged (see exemplary Figs. 3 and 4 for samples BST127 and BST641 and Table I for all investigated samples at $f = 3.3$ THz). This fact provides clear evidence that the photocurrent at normal incidence is dominated by the photogalvanic effect in the investigated 2D Dirac fermion systems. In samples BST127 and BST641 excited with $f = 2.0$ THz, the contribution of the photon drag is vanishingly small (see Fig. 3). At other frequencies and samples the photon drag effect may yield a contribution up to one third compared to that of the photogalvanic effect, resulting in larger signals for back illumination than for the front one [67] (see Fig. 4 and Table I).

So far we have presented data obtained for normal incidence. Illuminating the samples at oblique incidence, we found that all characteristic properties of the photocurrent, including its polarization behavior, remain unchanged (see Fig. 5). In contrast to the measurements at normal incidence, the magnitude $A_{x,y}(f,\theta)$ depends now additionally on the incident angle θ, as well as on the direction in which the current is examined: At large θ and for the plane of incidence coinciding, e.g., with the yz plane the photocurrent magnitudes measured in the x and y directions become slightly different. For some excitation frequencies the photocurrent amplitude $A_{x,y}(f,\theta)$ did decrease upon the increase of the angle θ, exemplarily shown for the current measured in the x direction in Figs. 5(a), 6(a), and 6(b). Note that the change of $A_{x,y}(f,\theta)$ is even in the angle θ.

Strikingly, at other radiation frequencies we observed that for positive as well as for negative θ the signal rises with an increase of the angle of incidence [see Figs. 5(b) and 6(c)–6(f)]. This behavior is observed for photocurrents measured in directions parallel as well as normal to the plane of incidence [see Fig. 6(d)]. It is also detected for any orientation of the plane of incidence. Figure 7 shows the corresponding data for three positions of the incident plane determined by the angle ψ. The figure reveals that the signal varies as $J_y = A_y(f,\psi)\sin(2\alpha - \phi)E_0^2$ and the most pronounced change in the photocurrents' polarization dependence is the appearance of a $\phi = 2\psi$ phase shift. A detected small variation of $A_y(f,\psi)$ as a function of ψ cannot be discussed earnestly since precise adjustment ensuring that, for different ψ, technically obtained by rotating the sample, the laser spot remains on the same sample position is hard to realize. To support the conclusion that the rotation of the incident plane results in a 2ψ phase shift, we measured photocurrents depending on the linear polarization by changing the angle ψ by steps of 10° in the range from 0° to 130°. Figure 8(a) demonstrates the dependencies obtained for Bi_2Te_3 sample BST127. The corresponding dependency of the measured phase shift ϕ on the angle ψ is shown in Fig. 8(b), and that for other samples and frequencies is shown in Fig. 8(c). The figures demonstrate that in all cases $\phi \approx 2\psi$.

Finally, we discuss the results obtained by applying elliptically (circularly) polarized radiation. These measurements were particularly motivated by the search for the circular photogalvanic [14,68,69] and circular photon drag effects [70,71], i.e., photocurrents changing their direction upon switching of the radiation helicity [10,11,13], recently observed for Bi_2Te_3

TI excited by near-infrared light [30]. Applying radiation at oblique incidence and measuring the photocurrent in the direction normal to the plane of incidence (yz), i.e., in the geometry for which circular photogalvanic [30,72,73] and circular photon drag effects [13,70] are expected, we detected a current which can be well fitted by $J_x = A_x(f)(\cos 4\varphi + 1)/2$ (see Fig. 9). Figure 9 clearly shows that for circularly polarized radiation ($\varphi = 45^\circ$ and 135°) the signal vanishes. In fact, the term in brackets describes the degree of linear polarization in the λ quarter-plate geometry. Therefore, the observed current is identical to the one excited by linearly polarized radiation, which was already discussed above. Examining different samples in the whole investigated THz frequency range, we observed the same result: No trace of a helicity-dependent photocurrent has been detected.

To summarize, experiments on different types of TI samples provide a self-consistent picture demonstrating that the photocurrents (i) are caused by effects proportional to the second power of the radiation electric field and can be excited by both normal and oblique incident radiation, (ii) are excited by linearly polarized radiation, (iii) vary with the azimuth angle α as $J \propto A(f,\theta,\psi)\sin 2\alpha$ with a possible phase shift depending on the experimental geometry and crystallographic direction in which the photocurrent is measured (see Figs. 7 and 8), (iv) have the same sign but may have distinct magnitudes of the factor $A(f)$ for front and back normal incident illumination (see Figs. 3 and 4), and (v) are described by an even function of the angle of incidence θ with the magnitude $A(f,\theta)$ for different radiation frequencies, increasing or decreasing with an increase of θ (see Figs. 5 and 6).

V. DISCUSSION

Now we discuss the origin of the observed photocurrents, which are induced by spatially homogeneous terahertz radiation and scale with the second power of the radiation electric field. We begin with the standard way to treat second-order effects without going into microscopic detail, which makes use of the symmetry arguments. This approach allows us to explore what kind of photocurrents are allowed in the considered system and to describe their variation upon a change of the macroscopic parameters, such as radiation intensity, polarization, and incident angle. With this, the response of the charge carriers ensemble to the external field can be characterized conveniently by the coordinate- and time-dependent electric current density $\boldsymbol{j}(\boldsymbol{r},t)$. It is expanded in a power series in the external alternating electric field $\boldsymbol{E}(\boldsymbol{r},t)$ in the form of a plane wave:

$$\boldsymbol{E}(\boldsymbol{r},t) = \boldsymbol{E}(\omega,\boldsymbol{q})e^{-i\omega t+i\boldsymbol{qr}} + \boldsymbol{E}^*(\omega,\boldsymbol{q})e^{i\omega t-i\boldsymbol{qr}}, \qquad (2)$$

where $\omega = 2\pi f$ is the angular frequency and $\boldsymbol{q}$ is its wave vector. Limiting the consideration to the second-order effects, we obtain the photocurrent density $j \propto J$ in the form [12,56]

$$j_\lambda = \sum_{\mu,\nu} \chi_{\lambda\mu\nu} E_\mu E_\nu^* + \sum_{\delta,\mu,\nu} T_{\lambda\delta\mu\nu} q_\delta E_\mu E_\nu^* + \text{c.c.}, \qquad (3)$$

where the expansion coefficients $\chi_{\lambda\mu\nu}$ and $T_{\lambda\mu\nu\delta}$ are third- and fourth-rank tensors, respectively, and $E_\nu^* = E_\nu^*(\omega) = E_\nu(-\omega)$ is the complex conjugate of E_ν. The first term on the right-hand side of Eq. (3) represents photogalvanic effects, whereas the second term describes the photon drag effect containing additionally the wave vector of the electromagnetic field. We emphasize that while the photogalvanic effect requires the absence of an inversion center and can be excited only in the surface states of the investigated TIs, a photon drag current can be generated in the centrosymmetric bulk as well. Moreover, in the case of the trigonal, the photon drag effect is described by the same phenomenological equations for bulk and surface states and therefore behaves identically upon variation of macroscopic parameters, such as radiation polarization.

Equation (3) can be simplified considering the point group C_{3v}, which describes the symmetry of the surface states in $(Bi_{1-x}Sb_x)_2Te_3$. To be specific we first obtain the photocurrents excited in the crystallographic directions x and y with the radiation plane of incidence (yz). Taking into account the fact that we detected only photocurrents excited by linearly polarized radiation that are even in the angle of incidence θ, we can omit all contributions of photocurrents sensitive to the radiation helicity and those giving a response that is odd in the angle θ. Under these conditions we derive for j

$$\begin{aligned} j_x &= (\chi + T_z q_z)\left(E_x^2 - E_y^2\right) - T_\parallel q_y E_y E_z \\ &= j^{\text{off}} - \cos 2\alpha\, E_0^2 \tfrac{1}{2}\left[(\chi - T_z q\cos\theta)\left(t_s^2 + t_p^2\cos^2\theta\right)\right. \\ &\quad \left. + T_\parallel q t_p^2 \sin^2\theta\cos\theta\right], \\ j_y &= -2(\chi + T_z q_z)E_x E_y - T_\parallel q_y E_x E_z \\ &= \sin 2\alpha\, t_s t_p[(\chi - T_z q\cos\theta)\cos\theta + T_\parallel q\sin^2\theta/2]E_0^2. \end{aligned} \qquad (4)$$

Here t_p and t_s are the Fresnel transmission coefficients for s- and p-polarized light, and j^{off} is the polarization-independent offset, which is equal to zero for $\theta = 0$ (see the Appendix). The constants χ, $T_\parallel$, and T_z are coefficients describing the photogalvanic effect, the photon drag effect at oblique incidence, and the photon drag effect at normal incidence, respectively.

At normal incidence we obtain the photogalvanic effect and the photon drag effect, caused by the z component of the photon wave vector. They are given, respectively, by the terms proportional to factors χ and T_z. Both effects have the same polarization dependence and vary with the azimuth angle α according to $j_x \propto (E_x^2 - E_y^2) \propto \cos 2\alpha$ and $j_y \propto 2E_x E_y \propto \sin 2\alpha$, in agreement with the results of experiments [see Figs. 3, 4, and Eq. (1)]. For $\chi \geqslant Tq_z$ reversing the radiation propagation direction ($\theta = 0 \Rightarrow \theta = 180^\circ$) does not affect the polarization dependence. It may, however, change the signal magnitude because $\chi + T_z q_z$ is different for negative and positive q_z, corresponding to front and back illumination. Exactly this behavior has been observed in experiments showing that at some frequencies the photon drag due to the z component of the wave vector yields a minor contribution to the total photocurrent (see values of J_x at $\theta = 0^\circ$ and 180° in Table I and Fig. 4). At oblique incidence the E_x and q_z components are reduced, and the magnitudes of both photocurrents diminish equally for positive and negative angle θ [see Fig. 5(a) and dotted lines in Fig. 6].

According to Eqs. (4), at oblique incidence the photon drag effect, coupled with the in-plane wave vector q_y, can also contribute to the total photocurrent. Its dependence on

the azimuth angle α formally coincides with that of the contributions discussed so far, $j_x \propto E_y E_z \propto \cos 2\alpha$ and $j_y \propto E_x E_z \propto \sin 2\alpha$. However, it obviously vanishes at normal incidence ($q_y = 0$) and, in contrast to the photogalvanic effect, increases with the rising angle of incidence (see dashed lines in Fig. 6). Moreover, the sign of the products $(E_y E_z q_y)$ and $(E_x E_z q_y)$ stays the same for positive and negative θ. A dominating contribution of this effect has been observed at large angles of incidence for all samples and for almost all frequencies. The most clear evidence for this conclusion is supported by measurements shown in Figs. 5(b) and 6(c)–6(f) demonstrate that the photocurrent rises with the increase of the angle θ.

Rotation of the incident plane by the angle ψ changes the relative orientation of the electric field and crystallographic axes, modifying Eqs. (4). Taking into account that in all experiments described above $T_\parallel q_y \gg (\chi + T_z q_z)$ and considering small angles θ, which is relevant to the experimental data of Figs. 5 and 6, we obtain

$$j_x \approx -\cos(2\alpha - 2\psi)(\chi - T_z q + T_\parallel q\theta^2/2)t^2 E_0^2,$$
$$j_y \approx \sin(2\alpha - 2\psi)(\chi - T_z q + T_\parallel q\theta^2/2)t^2 E_0^2. \quad (5)$$

Here $t = t_p = t_s$ is the amplitude of the transmission coefficient for small θ, and the offset current is omitted. Equations for an arbitrary angle of incidence are given in the Appendix. Equations (5) show that the rotation of the incident plane mainly results in a 2ψ phase shift for both photocurrents j_x and j_y. This phase shift has been observed for all samples and frequencies (see Figs. 7 and 8). While the above results were obtained while considering the point group C_{3v} of the surface states, our analysis shows that the same behavior of the photon drag current upon variation of radiation polarization, rotation of the plane of incidence, direction of radiation propagation, etc., is found for the bulk point-group symmetry D_{3d}. Therefore, in contrast to photogalvanics, this photocurrent can be attributed to surface states or the electron gas in the bulk only by a careful analysis of the influence of different microscopic parameters on the photocurrent behavior.

VI. MICROSCOPIC MODELS

In general, second-order high-frequency effects are caused by the redistribution of charge carriers in the momentum space induced by the illumination of the sample with radiation. The resulting nonequilibrium distribution can contain components which are oscillating in time and space, as well as steady-state and spatially homogeneous ones. Hence, the irradiation may cause both ac and dc flows in a medium. Their magnitudes are nonlinear functions of the field amplitude, and their components are sensitive to the radiation polarization. In the following section we present models visualizing the physics of nonlinear responses. For simplicity we assume positively charged carriers, i.e., holes for which the directions of the carrier flow and the corresponding electric current coincide.

A. Trigonal photogalvanic effect

The model and the microscopic theory of the photogalvanic effect have been discussed in detail in Ref. [19], demonstrating that the photocurrent stems from the asymmetric scattering of free carriers excited by irradiation with an ac electric field. As we show below, the asymmetric scattering is also responsible for the observed photon drag effects. Therefore, to introduce the concepts essential for the formation of the latter effects and to provide a complete picture of the photocurrent formation in TI, we will briefly address the model of the photogalvanic effect.

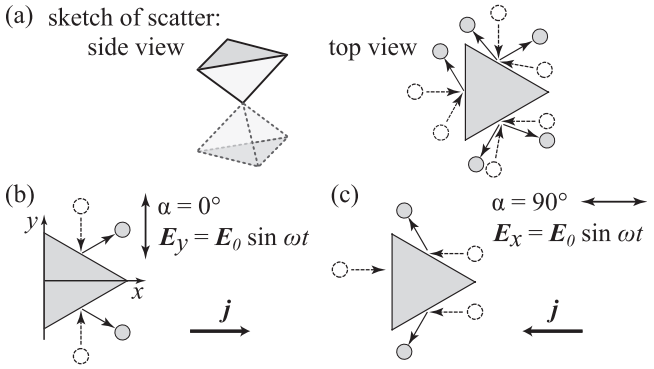

FIG. 10. Model of the photogalvanic effect, excited in surface states of $(Bi_{1-x}Sb_x)_2Te_3$ due to the asymmetry of elastic scattering of holes by wedges.

The current generation process is illustrated in Fig. 10. As addressed above, the symmetry of the surface states in $(Bi_{1-x}Sb_x)_2Te_3$ 3D TIs is C_{3v}. This point group implies that the anisotropy of carrier elastic scattering is the same as for scattering by a double triangular pyramid, whose side and top views are sketched in Fig. 10(a). Note that for C_{3v} symmetry scattering by the top and bottom pyramids has different probabilities. In the framework of the photogalvanic effect caused by the in-plane motion of free carriers the scatterers can be considered randomly distributed but identically oriented wedges lying in the QL plane. The preferential orientation of wedges is supported by the x-ray data shown above [see Fig. 2(a) and Refs. [19,74]]. In the absence of radiation, the flows of anisotropically scattered holes [see right panel Fig. 10(a)] exactly compensate each other. Application of linearly polarized THz radiation results in an *alignment* of carrier momenta: the total flow of holes driven back and forth by ac electric field $\boldsymbol{E}(t)$ increases. The corresponding *stationary* correction to the hole distribution function scales as a square of the ac electric field magnitude [75]. The *stationary alignment* of carrier momenta itself does not lead to a dc electric current, but due to asymmetric scattering by wedges, the excess of the flux of carriers moving along the field violates the balance of flows [73,76], and the linear photogalvanic current is generated [77]. The direction of the induced current depends on the relative orientation of the ac electric field and wedges: For example, a field parallel to the wedges' base [$\boldsymbol{E} \parallel y$; see Fig. 10(b)] yields the current flow in the x direction, while rotation of the electric field by 90° reverses the current direction [see Fig. 10(c)]. The polarization dependence of the photogalvanic current in the x and y directions is described by the terms with χ in Eqs. (5) and by Eq. (19). Note that the coefficient χ has opposite signs for holes and electrons.

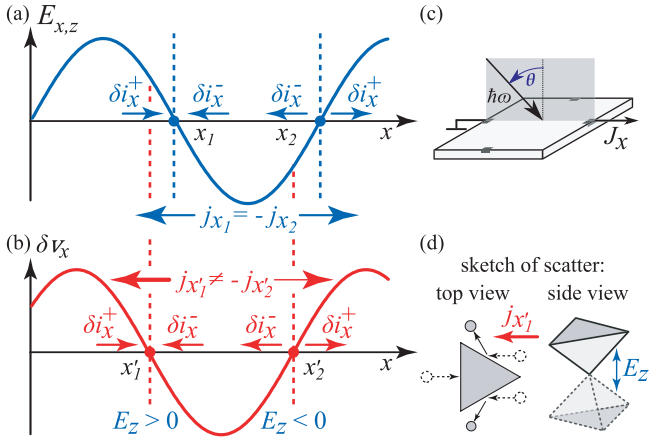

FIG. 11. Model of the trigonal photon drag effect caused by the in-plane wave vector q_x. To be specific, we discuss the hole gas in the surface states excited by oblique radiation with the incidence plane (xz); see (c). The triangle in the left picture in (d) shows the top view of the considered scattering potential. The side view of the scatters is sketched in the right picture.

B. Trigonal photon drag effects caused by the in-plane component of the photon wave vector

The trigonal photon drag effect caused by the in-plane component of the photon wave vector results in a dc current increasing with the increase of the angle of incidence. It is described by an *even* function of the angle θ. Similar to the photogalvanic effect, the photon drag current formation involves asymmetric scattering of free carriers and will be discussed in relation to the surface states. The model for the photon drag effect in the bulk is based on similar arguments but will not be further discussed here. The trigonal photon drag effect results from a *dynamical* alignment of carrier momenta. It is generated due to the in-plane profile of the radiation electric field and implies the difference in the scattering probabilities for different half periods of the electromagnetic wave. The process of the current generation is illustrated in Fig. 11. Like in the model for the photogalvanic effect, we consider the scatterers to be randomly distributed but identically oriented pyramids in the QL plane [see Fig. 11(d)]. In the absence of radiation, the flows of the thermalized charge carriers which are anisotropically scattered by pyramids exactly compensate each other. Optical excitation disturbs the balance due to the action of the high-frequency electric field $\boldsymbol{E}$ on charged carriers, we assume holes. The discussed trigonal photon drag current is caused by the dynamic variation of the electric field $\boldsymbol{E}$ in the direction of the radiation propagation [see Fig. 11(a)]. The strength of the corresponding force acting on holes is given by $|e|\boldsymbol{E}_\parallel e^{iq_\parallel r - i\omega t} \approx |e|i(\boldsymbol{q}_\parallel \boldsymbol{r})\boldsymbol{E}_\parallel e^{-i\omega t}$, where e is the elementary charge [13,78]. The force is coordinate dependent and causes the hole acceleration to be directed parallel to the x direction for $E_x > 0$ (antiparallel for $E_x < 0$) and, consequently, to increase the hole flow by δi_x^+ (δi_x^-) [see horizontal arrows in Fig. 11(a)]. As a result of this dynamical momentum alignment the balance of the hole flows scattered by pyramids in the vicinity of the electric field E_x nodes becomes *locally* violated [see Figs. 11(a) and 11(d)]. The asymmetric scattering may cause equal in magnitude but oppositely directed local electric currents j_{x_1} and j_{x_2} in the vicinity of x_1 and x_2, whereas the total electric current remains zero. However, steady-state dc electric current indeed emerges if one additionally takes into account the z component of the radiation field and the retardation between the electric field and the instant velocity of the charge carrier. The photocurrent reaches its maximum at $\omega\tau$ about unity. The effect of the retardation, well known in the Drude-Lorentz theory of high-frequency conductivity, causes a phase shift between the electric field E_x and the instant change of the hole velocity δv_x given by $\arctan(\omega\tau_{\rm tr})$. Consequently, the nodes of the charge-carrier velocity δv_x are shifted with respect to that of the electric field E_x; these nodes are indicated in Fig. 11(b) as x_1' and x_2'. The carriers in the vicinity of the x_1' and x_2' positions are subjected to the electric fields $E_z(x_1')$ and $E_z(x_2')$, which have opposite signs. The $E_z(x_1')$ $[E_z(x_2')]$ field is pushing the carriers to the base (top) of the pyramids, which increases (decreases) the scattering probability in the vicinity of x_1' (x_2'). Consequently, it changes the magnitudes of the local currents $j_{x_1'}$ and $j_{x_2'}$ caused by the asymmetric scattering. The variation of the scattering probability upon the action of the out-of-plane electric field $\delta W_{p'p}(E_z)$ is described by Eq. (11) in Sec. VII. As a result the oppositely directed local currents do not compensate each other anymore, and a dc electric current proportional to the product $q_x E_x E_z$ emerges. Changing the angle of incidence from θ to $-\theta$ reverses the sign of both q_x and the product $E_x E_z$ so that the direction of the dc current remains unchanged. We emphasize that such a contribution to the photon drag effect is specific to trigonal systems and it is absent in, e.g., hexagonal systems like graphene [13,71].

VII. MICROSCOPIC THEORY

Now we turn to the microscopic theory of the photon drag effect, presented in the surface states. In the classical regime achievable in our experiments, which is characterized by $\hbar\omega \ll \varepsilon_{\rm F}$, the photocurrents can be well described by means of Boltzmann's kinetic equation for the coordinate-dependent carrier distribution function $f_{\boldsymbol{p}}(\boldsymbol{r})$,

$$\left(\frac{\partial}{\partial t} + e\boldsymbol{E}(\boldsymbol{r},t)\cdot\frac{\partial}{\partial \boldsymbol{p}} + \boldsymbol{v}_{\boldsymbol{p}}\cdot\frac{\partial}{\partial \boldsymbol{r}}\right) f_{\boldsymbol{p}}(\boldsymbol{r}) = \sum_{\boldsymbol{p}'}[W_{\boldsymbol{p}\boldsymbol{p}'} f_{\boldsymbol{p}'}(\boldsymbol{r}) - W_{\boldsymbol{p}'\boldsymbol{p}} f_{\boldsymbol{p}}(\boldsymbol{r})], \tag{6}$$

where $e > 0$ for holes and $e < 0$ for electrons, $\boldsymbol{v}_{\boldsymbol{p}} = v_0\boldsymbol{p}/p$ is the velocity of surface charge carriers with a momentum $\boldsymbol{p}$, v_0 is the Dirac fermion velocity, and $W_{\boldsymbol{p}'\boldsymbol{p}}$ is the probability of a charge carrier having momenta $\boldsymbol{p}$ and $\boldsymbol{p}'$ before and after scattering, respectively. The lack of an inversion center for the surface charge carriers makes their elastic scattering asymmetric, so that $W_{\boldsymbol{p}\boldsymbol{p}'} \neq W_{-\boldsymbol{p},-\boldsymbol{p}'}$ [73,76], and a dc electric current results. Note that this asymmetry takes place even for isotropic scatterers like impurities or phonons. The photocurrent can be calculated as follows [12]:

$$\boldsymbol{j} = e\sum_{\boldsymbol{p}} \boldsymbol{v}_{\boldsymbol{p}}\delta f_{\boldsymbol{p}}\,, \tag{7}$$

where $\delta f_{\boldsymbol{p}}$ is the correction to the distribution function quadratic in the radiation electric field amplitude and linear in the photon momentum.

To calculate the asymmetric part of the scattering probability, which is responsible for the photocurrent formation, we take into account warping of the energy spectrum. Without warping, the energy dispersion of the surface states is described by the Hamiltonian [1]

$$H_0 = v_0(\sigma_x p_y - \sigma_y p_x), \tag{8}$$

where $\sigma_{x,y}$ are Pauli matrices. The Hamiltonian (8) yields the linear energy dispersion $\varepsilon_{e,h} = \pm v_0 p$ and corresponding wave functions $\Psi^{(0)}_{e,h} = [1, \mp i\exp(i\varphi_{\boldsymbol{p}})]/\sqrt{2}$ for electrons and holes, where $\varphi_{\boldsymbol{p}}$ is the angle between the carrier momentum $\boldsymbol{p}$ and the x axis. The warping of the energy spectrum reflects the trigonal symmetry of the surface and is described by, in addition to Eq. (8), a small term given by [79]

$$H_w = \lambda^w \sigma_z p^3 \sin 3\varphi_{\boldsymbol{p}}, \tag{9}$$

where λ^w is a warping constant. This is the perturbation which leads to the hexagonal warping of the energy surfaces [80] clearly detected by ARPES (see the top panels in Fig. 1).

The perturbation caused by the terahertz radiation electric field E_z changes the surface charge-carrier wave functions due to the admixture of bulk states from various bands. The corresponding Hamiltonian is linear in the coordinate z,

$$H_{em} = -ezE_z. \tag{10}$$

Taking into account both perturbations H_w and H_{em} in the first order, we obtain the corrected electron wave function:

$$\Psi_e = \Psi^{(0)}_e + \frac{\lambda^w p^2 \sin 3\varphi_{\boldsymbol{p}}}{2v_0}\Psi^{(0)}_h + eE_z \sum_n \frac{z_{ns}}{\varepsilon_n}\Psi_n,$$

where the index s labels the bulk orbitals from which the surface states are formed and n enumerates other energy bands of the bulk crystal. Here we assume that all bulk bands lie far enough away from the Dirac point so the energies $|\varepsilon_n| \gg \varepsilon_{\rm F} = v_0 p_{\rm F}$, where $p_{\rm F}$ is the Fermi momentum.

Calculating the matrix elements of scattering by a static potential, we obtain from Fermi's golden rule the scattering probability in the form $W_{\boldsymbol{p}'\boldsymbol{p}} = W^{(0)}_{\boldsymbol{p}'\boldsymbol{p}} + \delta W_{\boldsymbol{p}'\boldsymbol{p}}$. The field-independent part is given by the usual expression, taking into account the absence of back scattering for Dirac fermions [81]:

$$W^{(0)}_{\boldsymbol{p}'\boldsymbol{p}} = \frac{\pi}{\hbar}\langle|V(\boldsymbol{p}' - \boldsymbol{p})|^2\rangle(1 + \cos\theta_{\boldsymbol{p}'\boldsymbol{p}})\delta(v_0 p - v_0 p'),$$

where $V(\boldsymbol{p})$ is the Fourier image of the scattering potential, $\theta_{\boldsymbol{p}'\boldsymbol{p}} = \varphi_{\boldsymbol{p}'} - \varphi_{\boldsymbol{p}}$ is the scattering angle, and the angular brackets mean averaging over positions of scatterers [80]. The linear in E_z correction is given by

$$\delta W_{\boldsymbol{p}'\boldsymbol{p}} = \frac{2\pi}{\hbar}\delta(v_0 p - v_0 p')\sum_n \langle \mathrm{Im}(V_{sn} z_{ns} V^*_{ss})\rangle/\varepsilon_n \times eE_z \sin\theta_{\boldsymbol{p}'\boldsymbol{p}}\frac{\lambda p^2}{v_0}(\sin 3\varphi_{\boldsymbol{p}'} + \sin 3\varphi_{\boldsymbol{p}}). \tag{11}$$

Here V_{ss} and V_{sn} are the intra- and interband matrix elements of the scattering potential, respectively. The latter is caused by the short-range scatterers with the momentum transfer $\sim\hbar/a_0 \gg p_{\rm F}$, where a_0 has an atomic scale; therefore, the average product is assumed to be independent of $\varphi_{\boldsymbol{p}}$ and $\varphi_{\boldsymbol{p}'}$ [82]. We emphasize that the obtained correction, Eq. (11), is responsible for the effect of the E_z electric field on the scattering by pyramidlike scatters discussed in the model of the photon drag effect (see Sec. VI B).

Using the derived scattering probability $W_{\boldsymbol{p}'\boldsymbol{p}}$, we solve the Boltzmann equation (6) and obtain the $\boldsymbol{r}$-independent correction to the distribution function $\delta f_{\boldsymbol{p}}$, which allows us to calculate the photon drag current given by Eq. (7). For this we will search for the correction to the distribution function responsible for the *dynamical* alignment momentum $f^{(da)}_{\boldsymbol{p}}$. First, we find the linear in $\boldsymbol{E}_\parallel$ solution given by

$$f^{(E)}_{\boldsymbol{p}}(\boldsymbol{r}) = -\frac{df_0}{d\varepsilon_{\boldsymbol{p}}}\frac{e\tau_{\rm tr}}{1 - i\omega\tau_{\rm tr}}(\boldsymbol{E}_\parallel \cdot \boldsymbol{v}_{\boldsymbol{p}}), \tag{12}$$

where f_0 is the Fermi-Dirac distribution function and the transport relaxation time $\tau_{\rm tr}$ determining the mobility of 2D Dirac fermions is related to the symmetric part of the scattering probability as $\tau^{-1}_{\rm tr} = \sum_{\boldsymbol{p}'} W^{(0)}_{\boldsymbol{p}'\boldsymbol{p}}(1 - \cos\theta_{\boldsymbol{p}'\boldsymbol{p}})$. The photon wave vector is accounted for by the space derivatives in the kinetic equation [13]

$$\boldsymbol{v}_{\boldsymbol{p}} \cdot \frac{\partial f^{(E)}_{\boldsymbol{p}}}{\partial \boldsymbol{r}} = i(\boldsymbol{v}_{\boldsymbol{p}} \cdot \boldsymbol{q}) f^{(E)}_{\boldsymbol{p}} = \left(i\omega - \frac{1}{\tau_2}\right) f^{(da)}_{\boldsymbol{p}}. \tag{13}$$

The time τ_2, which is of the order of $\tau_{\rm tr}$, describes the relaxation of the above-discussed alignment of charge-carrier momenta. It is defined as follows:

$$\tau_2^{-1} = \sum_{\boldsymbol{p}'} W^{(0)}_{\boldsymbol{p}'\boldsymbol{p}}(1 - \cos 2\theta_{\boldsymbol{p}'\boldsymbol{p}}). \tag{14}$$

From Eq. (13) we find the correction to the distribution function describing the dynamical alignment of momenta in the form

$$f^{(da)}_{\boldsymbol{p}} = \frac{df_0}{d\varepsilon_{\boldsymbol{p}}} ie\tau_2\tau_{\rm tr}\frac{(\boldsymbol{v}_{\boldsymbol{p}} \cdot \boldsymbol{q})(\boldsymbol{E}_\parallel \cdot \boldsymbol{v}_{\boldsymbol{p}}) - (\boldsymbol{q} \cdot \boldsymbol{E}_\parallel)v^2_{\boldsymbol{p}}/2}{(1 - i\omega\tau_{\rm tr})(1 - i\omega\tau_2)}. \tag{15}$$

Now we take into account the anisotropic scattering which manifests as a correction given by Eq. (11). The $\boldsymbol{r}$-independent correction to the distribution function $\delta f_{\boldsymbol{p}}$ is found from the following equation [83]:

$$\sum_{\boldsymbol{p}'} \delta W_{\boldsymbol{p}'\boldsymbol{p}}\left(f^{(da)}_{\boldsymbol{p}} + f^{(da)}_{\boldsymbol{p}'}\right) = -\frac{\delta f_{\boldsymbol{p}}}{\tau_{\rm tr}}. \tag{16}$$

Finally, from Eq. (7) we find the trigonal photon drag current. Experiments reveal that the photocurrent in all samples is caused by the linearly polarized radiation. For excitation by oblique incidence in the (xz) plane it is described by

$$j_x = T_\parallel q_x E_x E_z = \frac{e\beta\lambda^w p^2_{\rm F}\omega\tau_2(\tau_{\rm tr} + \tau_2)}{4\left(1 + \omega^2\tau_2^2\right)}\sigma(\omega) q_x E_x E_z,$$
$$j_y = -T_\parallel q_x E_y E_z. \tag{17}$$

Here the high-frequency conductivity is given by the Drude expression for degenerate 2D carriers,

$$\sigma(\omega) = \frac{e^2\varepsilon_{\rm F}\tau_{\rm tr}}{4\pi\hbar^2\left(1 + \omega^2\tau^2_{\rm tr}\right)}.$$

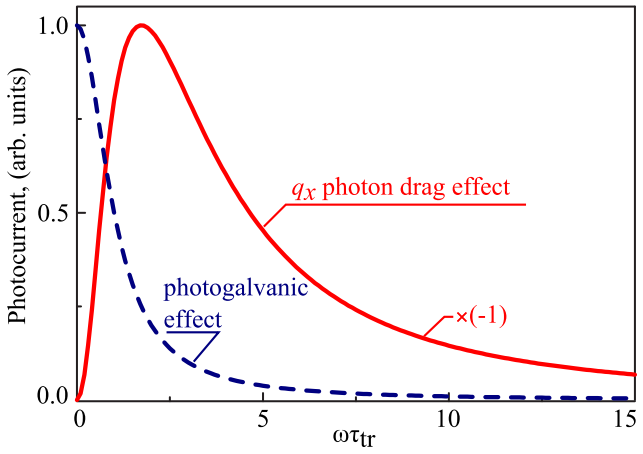

FIG. 12. Frequency dependencies for photogalvanic and photon drag photocurrents calculated after Eq. (19) (dashed curve) and Eq. (17) (solid curve), respectively. The curves are normalized by the corresponding photocurrent maximum. The photon drag current is multiplied by −1 because these terms always have, in experiments, the opposite sign.

We introduce the anisotropic scattering constant which is nonzero due to the C_{3v} symmetry of the studied system,

$$\beta = \frac{\sum_n \langle \mathrm{Im}(V_{sn} z_{ns} V_{ss}^*)\rangle/\varepsilon_n}{\langle |V(\boldsymbol{p}' - \boldsymbol{p})|^2 \sin^2\theta_{\boldsymbol{p}'\boldsymbol{p}}\rangle}, \tag{18}$$

where brackets in the denominator mean averaging over both scatterer positions and the scattering angle $\theta_{\boldsymbol{p}'\boldsymbol{p}}$. The derived Eqs. (17) show that, in line with experiments (see Fig. 6) and the discussion in Sec. V, the current is even in the angle of incidence and vanishes for normal incidence at which $q_x = 0$. For elastic scattering by Coulomb impurities, the relaxation times are related as $\tau_2 = \tau_{\mathrm{tr}}/3$. According to Ref. [19], in this case the photogalvanic current is given by

$$\begin{aligned} j_x &= \chi\left(E_x^2 - E_y^2\right) = e v_0 \frac{2\tau_{\mathrm{tr}}}{E_{\mathrm{F}}} \Xi\, \sigma(\omega)\left(E_x^2 - E_y^2\right), \\ j_y &= -2\chi E_x E_y, \end{aligned} \tag{19}$$

where Ξ is the factor describing the C_{3v} symmetry of the studied system. In the studied samples we can estimate $\Xi \sim 10^{-4}$–10^{-5} (see also Ref. [19]).

The frequency dependencies of trigonal photon drag and photogalvanic currents are plotted in Fig. 12. While photogalvanic current drops monotonously with an increase in frequency, the photon drag current has a maximum at $\omega\tau_{\mathrm{tr}} \approx 2$. At high frequencies, both linear photon drag and linear photogalvanic currents decrease as ω^{-2}. The difference between the frequency dependencies may be the cause for the observed variation of the ratio between photon drag and photogalvanic currents, which varies in the range from about −2 to −15 for different samples and frequencies.

The ratio of the photon drag and photogalvanic currents can be estimated as

$$T_\parallel q/\chi \sim \left(\lambda^w p_{\mathrm{F}}^2/v_0\right)(\beta q \varepsilon_{\mathrm{F}}/\Xi). \tag{20}$$

The first factor is a dimensionless degree of warping which can be of order of unity in our samples according to ARPES measurements (Fig. 1). In our experiments, the trigonal photon drag current at oblique incidence is larger than the photogalvanic one. This allows us to estimate the interband scattering parameter β defined by Eq. (18): in the studied samples $\beta > 10$ Å/eV. From the difference in sign between the photogalvanic and trigonal photon drag currents systematically observed in experiment we conclude that the products $\beta\lambda^w$, describing the trigonal photon drag and the photogalvanic constant Ξ, are of opposite sign. We note that since the photogalvanic effect is generated in the surface states with amplitudes comparable to those of the trigonal photon drag effect, we can draw the conclusion that the latter is also generated in the surface states. However, we do not find any straightforward experimental arguments to discriminate the contributions of the surface and bulk states in TIs with residual bulk conductivity. Moreover, these photon drag currents may be of the same magnitude because they are both determined by small radiation-induced corrections to the elastic scattering probability.

Finally, we note that the solution of the Boltzmann equation also yields the circular photon drag current proportional to the radiation helicity,

$$\begin{aligned} j_x^{\mathrm{circ}} &= -\frac{e\beta\lambda^w p_{\mathrm{F}}^2 \tau_2 (1 - \omega^2\tau_{\mathrm{tr}}\tau_2)}{4\left(1+\omega^2\tau_2^2\right)} \sigma(\omega) \frac{q_x q_y}{q} P_{\mathrm{circ}} t_s t_p |E_0|^2, \\ j_y^{\mathrm{circ}} &= \frac{e\beta\lambda^w p_{\mathrm{F}}^2 \tau_2 (1 - \omega^2\tau_{\mathrm{tr}}\tau_2)}{8\left(1+\omega^2\tau_2^2\right)} \sigma(\omega) \frac{q_x^2 - q_y^2}{q} P_{\mathrm{circ}} t_s t_p |E_0|^2. \end{aligned} \tag{21}$$

It follows from these expressions that the circular photon drag current is zero at $\omega\tau_{\mathrm{tr}} \approx 1$, a value at which the linear photon drag current is close to its maximum (Fig. 12). The vanishing contribution of the circular photocurrent in the vicinity of $\omega\tau_{\mathrm{tr}} \approx 1$, the condition corresponding to our experiments, may explain the fact that in the studied frequency range no helicity-dependent current has been detected.

Microscopic theory of the photon drag effect due to the q_z component of the photon wave vector

Last but not least, we obtain the trigonal photon drag current caused by the q_z component of the photon wave vector. It is given by

$$\begin{aligned} j_x &= T_z q_z (|E_x|^2 - |E_y|^2), \\ j_y &= -T_z q_z (E_x E_y^* + E_y E_x^*), \end{aligned} \tag{22}$$

where T_z is a real constant. The equations reveal that the photocurrent can be excited by linearly polarized radiation and is sensitive to the polarization plane position with respect to the crystallographic axes.

The microscopic picture of the photocurrent generation can most conveniently be described in terms of the radiation magnetic field $\boldsymbol{B}$ rather than the transfer of the normal component of the photon wave vector q_z to free carriers. Indeed, the latter is not possible in strictly 2D systems. Using the relation $\boldsymbol{B} = (c/\omega)\boldsymbol{q}\times\boldsymbol{E}$, we can rewrite Eq. (22) as $j_x \propto E_x B_y^* + E_y B_x^* + \mathrm{c.c.}$ and $j_y \propto E_x B_x^* - E_y B_y^* + \mathrm{c.c.}$

In order to develop a microscopic theory for the photocurrent given by Eq. (22), we take into account the Lorentz force

of the radiation magnetic field acting on the 2D carriers. The corresponding Hamiltonian has the following form:

$$H_{\boldsymbol{B}} = \frac{ez}{m_0 c}(B_x p_y - B_y p_x). \tag{23}$$

Taking into account both $H_{\boldsymbol{B}}$ and the warping perturbation Eq. (9) in the first order, we derive the linear in $\boldsymbol{B}$ correction to the elastic scattering probability $\delta W^{(\boldsymbol{B})}_{\boldsymbol{p}'\boldsymbol{p}}$. It is obtained from $\delta W_{\boldsymbol{p}'\boldsymbol{p}}$, Eq. (11), by substitution,

$$E_z \to \frac{1}{m_0 c}[B_y(p_x + p'_x) - B_x(p_y + p'_y)].$$

Now we solve the Boltzmann kinetic equation (6) accounting for the correction $\delta W^{(\boldsymbol{B})}_{\boldsymbol{p}'\boldsymbol{p}}$ to the scattering probability. It has the form

$$\sum_{\boldsymbol{p}'} \delta W^{(\boldsymbol{B})}_{\boldsymbol{p}'\boldsymbol{p}}\left(f^{(E)}_{\boldsymbol{p}} - f^{(E)}_{\boldsymbol{p}'}\right) = -\frac{\delta f^{(\boldsymbol{B})}_{\boldsymbol{p}}}{\tau_{\rm tr}}, \tag{24}$$

where $\delta f^{(\boldsymbol{B})}_{\boldsymbol{p}}$ is the correction to the distribution function linear in $\boldsymbol{B}$ and the linear in $\boldsymbol{E}_\parallel$ correction $f^{(E)}_{\boldsymbol{p}}(\boldsymbol{r})$ is given by Eq. (12).

The current density linear in both $\boldsymbol{E}_\parallel$ and $\boldsymbol{B}_\parallel$ is calculated by Eq. (7) with the above correction $\delta f^{(\boldsymbol{B})}_{\boldsymbol{p}}$. The result has the form

$$j_x = T_z q_z\left(E_x^2 - E_y^2\right) = -\frac{e\beta\lambda p_{\rm F}^2 \varepsilon_{\rm F}}{4\omega m_0 v_0^2}\sigma(\omega) q_z\left(E_x^2 - E_y^2\right),$$
$$j_y = -2T_z q_z E_x E_y. \tag{25}$$

Comparing the photocurrent amplitudes at normal and oblique incidence, Eqs. (17) and (25), we obtain

$$T_z/T_\parallel \sim \frac{1 + (\omega\tau_{\rm tr})^2}{(\omega\tau_{\rm tr})^2}\frac{\varepsilon_{\rm F}}{m_0 v_0^2}. \tag{26}$$

This estimate demonstrates that, because the radiation magnetic field affects elastic scattering weaker than the electric field, T_z is substantially smaller than $T_\parallel$. Since $m_0 v_0^2 \sim 10$ eV, the factor $\varepsilon_{\rm F}/m_0 v_0^2$ is on the order of 10^{-1} to 10^{-2} for our samples. This estimation explains why in all our experiments $T_\parallel \gg T_z$. The smallest values of $T_\parallel/T_z$ obtained are 40 times for sample BST127 and 80 for sample BST641. In both cases the samples were excited by radiation of $f = 3.3$ THz. For other conditions the ratio was even larger, or the q_z-related photon drag contribution was not detectable. The only reason why we were able to detect such a small contribution at all is that photon drag due to the in-plane wave vector vanishes at normal incidence, whereas that caused by the q_z component achieves its maximum. Finally, we note that constant T_z has a frequency dependence different from that of $T_\parallel$. In particular, the role of the q_z-photon drag current is enhanced at small frequencies, $\omega\tau_{\rm tr} \ll 1$.

VIII. CONCLUSION

To summarize, our experiments on a large set of n- and p-type $(Bi_{1-x}Sb_x)_2Te_3$ three-dimensional topological insulators demonstrated that normal incident THz radiation results in the photogalvanic current induced in the surface states. At oblique incidence, however, in particular at large angles of incidence, it is outweighed by the photon drag effect. The microscopic model and theory developed show that the photon drag photocurrent is caused by the *dynamical* momentum alignment by the time- and space-dependent radiation electric field and imply the difference in the scattering probabilities for different half periods of the electromagnetic wave. Both photocurrents observed even at room temperature stem from scattering events and therefore can be applied to study the high-frequency conductivity in TI.

ACKNOWLEDGMENTS

We thank M. M. Glazov and S. A. Tarasenko for fruitful discussions. The support from the DFG priority program SPP1666 and the Virtual Institute for Topological Insulators, the Elite Network of Bavaria (K-NW-2013-247), and the Russian Foundation of Basic Research is gratefully acknowledged.

APPENDIX

Phenomenological analysis of the C_{3v} symmetry at linear polarization of radiation accounting for the photogalvanic and photon drag effects yields even in θ photocurrents (4), which can be conveniently written in the following form:

$$j_x + ij_y = (\chi + T_z q_z)(E_x - iE_y)^2 + T_\parallel(q_x - iq_y)(E_x - iE_y)E_z. \tag{A1}$$

We consider oblique incidence with an incidence plane at an angle ψ with the yz plane, and α is an angle between the radiation electric vector and the incidence plane ($\alpha = 0$ corresponds to p polarization). In these notations we have

$$q_x - iq_y = -iq\sin\theta e^{-i\psi}, \quad q_z = -q\cos\theta, \tag{A2}$$

$$E_x - iE_y = -(t_s\sin\alpha + it_p\cos\alpha\cos\theta)E_0 e^{-i\psi}, \tag{A3}$$

$$E_z = t_p E_0\sin\theta\sin\alpha. \tag{A4}$$

Here E_0 is the electric field amplitude in vacuum, and t_s, t_p are Fresnel transmission coefficients for s and p polarizations.

Substitution of the wave vector and electric field components into Eq. (A1) yields the photocurrent in the following form:

$$j_x = j^{\rm off} - \cos(2\alpha - \gamma)\sqrt{(A_c\cos 2\psi)^2 + (A_s\sin 2\psi)^2}E_0^2, \tag{A5}$$

$$j_y = \sin(2\alpha - \gamma')\sqrt{(A_s\cos 2\psi)^2 + (A_c\sin 2\psi)^2}E_0^2. \tag{A6}$$

Here the amplitudes are functions of the incidence angle,

$$A_c = \tfrac{1}{2}\left[(\chi - T_z q\cos\theta)\left(t_s^2 + t_p^2\cos^2\theta\right) + T_\parallel q t_p^2\sin^2\theta\cos\theta\right], \tag{A7}$$

$$A_s = t_s t_p\cos\theta(\chi - T_z q\cos\theta) + T_\parallel q t_s t_p\sin^2\theta/2, \tag{A8}$$

the phase shifts are given by

$$\tan\gamma = \frac{A_s}{A_c}\tan 2\psi, \quad \tan\gamma' = \frac{A_c}{A_s}\tan 2\psi, \tag{A9}$$

and the α-independent offset photocurrent is

$$j^{\text{off}} = -\frac{\sin^2\theta}{2}\left[(\chi - T_z q\cos\theta) f(\theta) + T_\parallel q t_p^2 \cos\theta\right] E_0^2, \tag{A10}$$

where

$$f(\theta) \equiv \frac{t_p^2\cos^2\theta - t_s^2}{\sin^2\theta} = \frac{t_s t_p (t_p\cos\theta + t_s)}{2\cos\theta}\left[1 + \frac{n\cos\theta - 1}{n^2(1+\sqrt{1-\sin^2\theta/n^2})}\right]. \tag{A11}$$

Taking into account that in our structures $T_\parallel q \gg \chi, T_z q$, we have at small θ

$$j_x = -\cos(2\alpha - 2\psi)(\chi - T_z q + T_\parallel q\theta^2/2) t^2 E_0^2 + j^{\text{off}}, \tag{A12}$$

$$j_y = \sin(2\alpha - 2\psi)(\chi - T_z q + T_\parallel q\theta^2/2) t^2 E_0^2. \tag{A13}$$

Here t is the amplitude transmission coefficient for normal incidence, and

$$j^{\text{off}} = -T_\parallel q\theta^2 t^2 E_0^2/2. \tag{A14}$$

[1] M. Z. Hasan and C. L. Kane, Rev. Mod. Phys. **82**, 3045 (2010).
[2] J. E. Moore, Nature (London) **464**, 194 (2010).
[3] X. L. Qi and S. C. Zhang, Rev. Mod. Phys. **83**, 1057 (2011).
[4] J. H. Bardarson and J. E. Moore, Rep. Prog. Phys. **76**, 056501 (2013).
[5] B. A. Bernevig and T. L. Hughes, *Topological Insulators and Superconductors* (Princeton University Press Group, Woodstock, UK, 2013).
[6] *Topological Insulators Contemporary Concepts of Condensed Matter Science*, edited by M. Franz and L. Molenkamp (Elsevier, Oxford, 2013).
[7] S.-Q. Shen, *Topological Insulators: Dirac Equation in Condensed Matters*, Springer Series in Solid-State Sciences (Springer, Berlin, 2013).
[8] F. Ortmann, S. Roche, and S. O. Valenzuela, *Topological Insulators: Fundamentals and Perspectives* (Wiley-VCH, Weinheim, 2015).
[9] *Topological Insulators: The Physics of Spin Helicity in Quantum Transport*, edited by Gregory Tkachov (Pan Stanford, Singapore, 2015).
[10] S. D. Ganichev and W. Prettl, J. Phys.: Condens. Matter **15**, R935 (2003).
[11] E. L. Ivchenko and S. D. Ganichev, *Spin Photogalvanics in Spin Physics in Semiconductors*, edited by M. I. Dyakonov (Springer, Berlin, Heidelberg, 2008).
[12] E. L. Ivchenko, *Optical Spectroscopy of Semiconductor Nanostructures* (Alpha Science, Harrow, UK, 2005).
[13] M. M. Glazov and S. D. Ganichev, Phys. Rep. **535**, 101 (2014).
[14] P. Hosur, Phys. Rev. B **83**, 035309 (2011).
[15] J. W. McIver, D. Hsieh, H. Steinberg, P. Jarillo-Herrero, and N. Gedik, Nat. Nanotechnol. **7**, 96 (2012).
[16] A. Junck, G. Refael, and F. von Oppen, Phys. Rev. B **88**, 075144 (2013).
[17] J. Duan, N. Tang, X. He, Y. Yan, S. Zhang, X. Qin, X. Wang, X. Yang, F. Xu, Y. Chen, W. Ge, and B. Shen, Sci. Rep. **4**, 4889 (2014).
[18] A. M. Shikin, A. A. Rybkina, I. I. Klimovskikh, M. V. Filianina, K. A. Kokh, O. E. Tereshchenko, P. N. Skirdkov, K. A. Zvezdin, and A. K. Zvezdin, arXiv:1511.05663.
[19] P. Olbrich, L. E. Golub, T. Herrmann, S. N. Danilov, H. Plank, V. V. Bel'kov, G. Mussler, Ch. Weyrich, C. M. Schneider, J. Kampmeier, D. Grützmacher, L. Plucinski, M. Eschbach, and S. D. Ganichev, Phys. Rev. Lett. **113**, 096601 (2014).
[20] L. Braun, G. Mussler, A. Hruban, M. Konczykowski, M. Wolf, T. Schumann, M. Münzenberg, L. Perfetti, and T. Kampfrath, arXiv:1511.00482.
[21] L.-G. Zhu, B. Kubera, K. F. Mak, and J. Shan, Sci. Rep. **5**, 10308 (2015).
[22] Ch. Kastl, T. Guan, X. Y. He, K. H. Wu, Y. Q. Li, and A. W. Holleitner, Appl. Phys. Lett. **101**, 251110 (2012).
[23] Ch. Kastl, Ch. Karnetzky, H. Karl, and A. W. Holleitner, Nat. Commun. **6**, 6617 (2015).
[24] Z. D. Kvon, K.-M. Dantscher, C. Zoth, D. A. Kozlov, N. N. Mikhailov, S. A. Dvoretsky, and S. D. Ganichev, JETP Lett. **99**, 290 (2014).
[25] V. Kaladzhyan, P. P. Aseev, and S. N. Artemenko, Phys. Rev. B **92**, 155424 (2015).
[26] D. A. Bas, K. Vargas-Velez, S. Babakiray, T. A. Johnson, P. Borisov, T. D. Stanescu, D. Lederman, and A. D. Bristow, Appl. Phys. Lett. **106**, 041109 (2015).
[27] R. A. Muniz and J. E. Sipe, Phys. Rev. B **89**, 205113 (2014).
[28] Y. Onishi, Z. Ren, M. Novak, K. Segawa, Y. Ando, and K. Tanaka, arXiv:1403.2492.
[29] H. C. Lee, Phys. E (Amsterdam, Neth.) **79**, 44 (2016).
[30] J. W. McIver, D. Hsieh, S. G. Drapcho, D. H. Torchinsky, D. R. Gardner, Y. S. Lee, and N. Gedik, Phys. Rev. B **86**, 035327 (2012).
[31] T. Kitagawa, T. Oka, A. Brataas, L. Fu, and E. Demler, Phys. Rev. B **84**, 235108 (2011).
[32] B. Dora, J. Cayssol, F. Simon, and R. Moessner, Phys. Rev. Lett. **108**, 056602 (2012).
[33] P. Olbrich, C. Zoth, P. Vierling, K.-M. Dantscher, G. V. Budkin, S. A. Tarasenko, V. V. Bel'kov, D. A. Kozlov, Z. D. Kvon, N. N. Mikhailov, S. A. Dvoretsky, and S. D. Ganichev, Phys. Rev. B **87**, 235439 (2013).
[34] K.-M. Dantscher, D. A. Kozlov, P. Olbrich, C. Zoth, P. Faltermeier, M. Lindner, G. V. Budkin, S. A. Tarasenko, V. V. Bel'kov, Z. D. Kvon, N. N. Mikhailov, S. A. Dvoretsky, D. Weiss, B. Jenichen, and S. D. Ganichev, Phys. Rev. B **92**, 165314 (2015).
[35] C. Zoth, P. Olbrich, P. Vierling, K.-M. Dantscher, V. V. Bel'kov, M. A. Semina, M. M. Glazov, L. E. Golub, D. A. Kozlov, Z. D. Kvon, N. N. Mikhailov, S. A. Dvoretsky, and S. D. Ganichev, Phys. Rev. B **90**, 205415 (2014).

[36] Y. G. Semenov, X. Li, and K. W. Kim, Phys. Rev. B **86**, 201401 (2012).
[37] X. Li, Yu. G. Semenov, and K. W. Kim, Appl. Phys. Lett. **104**, 061116 (2014).
[38] J. D. Yao, J. M. Shao, S. W. Li, D. H. Bao, and G. W. Yang, Sci. Rep. **5**, 14184 (2015).
[39] S. G. Egorova, V. I. Chernichkin, L. I. Ryabova, E. P. Skipetrov, L. V. Yashina, S. N. Danilov, S. D. Ganichev, and D. R. Khokhlov, Sci. Rep. **5**, 11540 (2015).
[40] J. G. Checkelsky, Y. S. Hor, M. H. Liu, D. X. Qu, R. J. Cava, and N. P. Ong, Phys. Rev. Lett. **103**, 246601 (2009).
[41] A. A. Taskin and Y. Ando, Phys. Rev. B **80**, 085303 (2009).
[42] J. G. Analytis, J. H. Chu, Y. Chen, F. Corredor, R. D. McDonald, Z. X. Shen, and I. R. Fisher, Phys. Rev. B **81**, 205407 (2010).
[43] L. Barreto, L. Kühnemund, F. Edler, Ch. Tegenkamp, J. Mi, M. Bremholm, B. B. Iversen, Ch. Frydendahl, M. Bianchi, and P. Hofmann, Nano Lett. **14**, 3755 (2014).
[44] Z. Ren, A. A. Taskin, S. Sasaki, K. Segawa, and Y. Ando, Phys. Rev. B **82**, 241306 (2010).
[45] D.-X. Qu, Y. S. Hor, J. Xiong, R. J. Cava, and N. P. Ong, Science **329**, 821 (2010)
[46] J. Zhang, C.-Z. Chang, Z. Zhang, J. Wen, X. Feng, K. Li, M. Liu, K. He, L. Wang, W. Chen, Q.-K. Xue, and X. M. Wang, Nat. Commun. **2**, 574 (2011).
[47] C. Weyrich, M. Drögeler, J. Kampmeier, M. Eschbach, G. Mussler, T. Merzenich, T. Stoica, I. E. Batov, J. Schubert, L. Plucinski, B. Beschoten, C. M. Schneider, and C. Stampfer, D. Grützmacher, and Th. Schäpers, arXiv:1511.00965.
[48] M. Eschbach, E. Młyńczak, J. Kellner, J. Kampmeier, M. Lanius, E. Neumann, C. Weyrich, M. Gehlmann, P. Gospodarič, S. Döring, G. Mussler, N. Demarina, M. Luysberg, G. Bihlmayer, Th. Schäpers, L. Plucinski, S. Blügel, M. Morgenstern, C. M. Schneider, and D. Grützmacher, Nat. Commun. **6**, 8816 (2015).
[49] Y. Liu, M. Weinert, and L. Li, Phys. Rev. Lett **108**, 115501 (2012).
[50] S. Borisova, J. Krumrain, M. Luysberg, G. Mussler, and D. Grützmacher, Cryst. Growth Des. **12**, 6098 (2012).
[51] S. Borisova, J. Kampmeier, M. Luysberg, G. Mussler, and D. Grützmacher, Appl. Phys. Lett. **103**, 081902 (2013).
[52] L. Plucinski, A. Herdt, S. Fahrendorf, G. Bihlmayer, G. Mussler, S. Döring, J. Kampmeier, F. Matthes, D. E. Bürgler, D. Grützmacher, S. Blügel, and C. M. Schneider, Appl. Phys. **113**, 053706 (2013).
[53] Y. Xia, D. Qian, D. Hsieh, L. Wray, A. Pal, H. Lin, A. Bansil, D. Grauer, Y. S. Hor, R. J. Cava, and M. Z. Hasan, Nat. Phys. **5**, 398 (2009).
[54] D. Hsieh, Y. Xia, D. Qian, L. Wray, J. H. Dil, F. Meier, J. Osterwalder, L. Patthey, J. G. Checkelsky, N. P. Ong, A. V. Fedorov, H. Lin, A. Bansil, D. Grauer, Y. S. Hor, R. J. Cava, and M. Z. Hasan, Nature (London) **460**, 1101 (2009).
[55] J. Kampmeier, S. Borisova, L. Plucinski, M. Luysberg, G. Mussler, and D. Grützmacher, Cryst. Growth Des. **15**, 390 (2015).
[56] S. D. Ganichev and W. Prettl, *Intense Terahertz Excitation of Semiconductors* (Oxford University Press, Oxford, 2006).
[57] C. Drexler, S. A. Tarasenko, P. Olbrich, J. Karch, M. Hirmer, F. Müller, M. Gmitra, J. Fabian, R. Yakimova, S. Lara-Avila, S. Kubatkin, and S. D. Ganichev, Nat. Nanotechnol. **8**, 104 (2013).
[58] S. D. Ganichev, W. Prettl, and P. G. Huggard, Phys. Rev. Lett. **71**, 3882 (1993).
[59] S. D. Ganichev, I. N. Yassievich, W. Prettl, J. Diener, B. K. Meyer, and K. W. Benz, Phys. Rev. Lett. **75**, 1590 (1995).
[60] S. D. Ganichev, E. Ziemann, Th. Gleim, W. Prettl, I. N. Yassievich, V. I. Perel, I. Wilke, and E. E. Haller, Phys. Rev. Lett. **80**, 2409 (1998).
[61] P. Olbrich, E. L. Ivchenko, R. Ravash, T. Feil, S. D. Danilov, J. Allerdings, D. Weiss, D. Schuh, W. Wegscheider, and S. D. Ganichev, Phys. Rev. Lett. **103**, 090603 (2009).
[62] V. Lechner, L. E. Golub, P. Olbrich, S. Stachel, D. Schuh, W. Wegscheider, V. V. Bel'kov, and S. D. Ganichev, Appl. Phys. Lett. **94**, 242109 (2009).
[63] S. D. Ganichev, Y. V. Terent'ev, and I. D. Yaroshetskii, Pis'ma Zh. Tekh. Fiz. **11**, 46 (1985) [Sov. Tech. Phys. Lett. **11**, 20 (1985)].
[64] V. V. Bel'kov and S. D. Ganichev, Semicond. Sci. Technol. **23**, 114003 (2008).
[65] S. D. Ganichev, S. A. Tarasenko, V. V. Bel'kov, P. Olbrich, W. Eder, D. R. Yakovlev, V. Kolkovsky, W. Zaleszczyk, G. Karczewski, T. Wojtowicz, and D. Weiss, Phys. Rev. Lett. **102**, 156602 (2009).
[66] The polarization-independent offsets C and C', which are in most samples much smaller than $A(f)$, may be caused by the non-perfectly-flat surface, which locally reduces the symmetry of the surface states and allows a polarization-independent contribution to both effects [19].
[67] The difference in the photocurrent magnitudes $A(f)$ for front and back illuminations may be additionally affected by the unequal photocurrent contributions excited in the top and interface surfaces separated by the bulk material, e.g., due to different scattering times.
[68] S. D. Ganichev, V. V. Bel'kov, P. Schneider, E. L. Ivchenko, S. A. Tarasenko, W. Wegscheider, D. Weiss, D. Schuh, E. V. Beregulin, and W. Prettl, Phys. Rev. B **68**, 035319 (2003).
[69] S. D. Ganichev, P. Schneider, V. V. Bel'kov, E. L. Ivchenko, S. A. Tarasenko, W. Wegscheider, D. Weiss, D. Schuh, B. N. Murdin, P. J. Phillips, C. R. Pidgeon, D. G. Clarke, M. Merrick, P. Murzyn, E. V. Beregulin, and W. Prettl, Phys. Rev. B **68**, 081302(R) (2003).
[70] H. Diehl, V. A. Shalygin, V. V. Bel'kov, Ch. Hoffmann, S. N. Danilov, T. Herrle, S. A. Tarasenko, D. Schuh, Ch. Gerl, W. Wegscheider, W. Prettl, and S. D. Ganichev, New J. Phys. **9**, 349 (2007).
[71] J. Karch, P. Olbrich, M. Schmalzbauer, C. Zoth, C. Brinsteiner, M. Fehrenbacher, U. Wurstbauer, M. M. Glazov, S. A. Tarasenko, E. L. Ivchenko, D. Weiss, J. Eroms, R. Yakimova, S. Lara-Avila, S. Kubatkin, and S. D. Ganichev, Phys. Rev. Lett. **105**, 227402 (2010).
[72] S. D. Ganichev, E. L. Ivchenko, and W. Prettl, Phys. E (Amsterdam, Neth.) **14**, 166 (2002).
[73] W. Weber, L. E. Golub, S. N. Danilov, J. Karch, C. Reitmaier, B. Wittmann, V. V. Bel'kov, E. L. Ivchenko, Z. D. Kvon, N. Q. Vinh, A. F. G. van der Meer, B. Murdin, and S. D. Ganichev, Phys. Rev. B **77**, 245304 (2008).
[74] H. Zhang, C.-X. Liu, X.-L. Qi, X. Dai, Z. Fang, and S.-C. Zhang, Nat. Phys. **5**, 438 (2009).
[75] The stationary correction to the distribution function $f_p(t)$ is obtained by writing it as an expansion in powers of the electric

field $f_{\boldsymbol{p}}(t) = f_0 + f_{\boldsymbol{p}}^{(1)}(t) + f_{\boldsymbol{p}}^{(2)}$ with the oscillating in time term $f_{\boldsymbol{p}}^{(1)}(t) \propto \exp(-i\omega t)$ and the stationary term $f_{\boldsymbol{p}}^{(2)} \propto |\boldsymbol{E}|^2$ being second order in the electric field.

[76] V. I. Belinicher and B. I. Sturman, Sov. Phys. Usp. **23**, 199 (1980).

[77] The oscillating in time term $f_{\boldsymbol{p}}^{(1)}(t)$ (see [75]) does not disturb the balance of scattered carriers and, consequently, does not results in a dc current.

[78] V. I. Perel' and Ya. M. Pinskii, Fiz. Tverd. Tela **15**, 996 (1973) [Sov. Phys. Solid State **15,** 688 (1973)].

[79] L. Fu, Phys. Rev. Lett. **103**, 266801 (2009).

[80] Note that, in spite of the fact that $H_w \propto \lambda^w$, the correction to the electron energy is quadratic in λ^w because linear in λ^w terms are forbidden by time-inversion symmetry, so that $\delta\varepsilon_{\boldsymbol{p}} = -[(\lambda^w)^2 p^5/4v_0]\cos 6\varphi_{\boldsymbol{p}}$.

[81] S. Das Sarma, S. Adam, E. H. Hwang, and E. Rossi, Rev. Mod. Phys. **83**, 407 (2011).

[82] S. A. Tarasenko, Phys. Rev. B **83**, 035313 (2011).

[83] Note that if one first takes into account $\delta W_{\boldsymbol{p}'\boldsymbol{p}}$, then the correction to the distribution function contains $E_z E_x^*$-like bilinear combinations of the electric field amplitudes which are $\boldsymbol{r}$ independent, and hence, its gradient is zero.